Biomedical Signal Processing and Control 125 (2026) 110761

Contents lists available at ScienceDirect

Biomedical Signal Processing and Control

journal homepage: www.elsevier.com/locate/bspc

Memristor-driven spike encoding for fully implantable cochlear implants

Tímea Nóra Török [a,b,*], Roland Kövecs [a], Ferenc Braun [b], Zsigmond Pollner [a,c], Tamás Zeffer [b,d], Nguyen Quoc Khánh [b], László Pósa [a,b], Péter Révész [e], Heungsoo Kim [f], Alberto Piqué [f], András Halbritter [a,c], János Volk [b]

[a] Department of Physics, Institute of Physics, Budapest University of Technology and Economics, Műegyetem rkp. 3., Budapest, H-1111, Hungary
[b] Institute of Technical Physics and Materials Science, HUN-REN Centre for Energy Research, Konkoly-Thege M. út 29-33., Budapest, H-1121, Hungary
[c] HUN-REN-BME Condensed Matter Research Group, Budapest University of Technology and Economics, Műegyetem rkp. 3., Budapest, H-1111, Hungary
[d] Doctoral School on Material Sciences & Technologies, Óbuda University, Bécsi str. 96/b, Budapest, H-1034, Hungary
[e] Department of Otorhinolaryngology–Head and Neck Surgery, Clinical Center, University of Pécs, Munkácsy M. u. 2, Pécs, H-7621, Hungary
[f] Naval Research Laboratory, 4555 Overlook Ave, Washington, DC, 20375, USA

ARTICLE INFO

Dataset link: https://hdl.handle.net/21.15109/ARP/NNEEQB

Keywords:
Action potential
Frequency resolved MEMS array
Nanogap memristor
Piezo-MEMS
Rate encoding
Tonotopy
VO_2

ABSTRACT

Neurodynamic behavior of artificial neuron circuits made of Mott memristors provides versatile opportunities to utilize them for artificial sensing. Their compactness and energy-efficient spike generation enable integration into medical implants. This work demonstrates a low-power, biomimetic auditory sensing concept for fully implantable cochlear implants. The approach draws inspiration from the frequency selectivity and temporal encoding of the cochlea, and uses neuromorphic spike generation to replace conventional signal processing blocks. The auditory sensing unit is realized by a piezoelectric MEMS cantilever coupled to a single VO_2 nanogap Mott memristor-based oscillator. This configuration enables FFT-free, frequency-selective sensing and direct spike generation, forming a biomimetic auditory front end. The sensing unit exhibits frequency-selective detection of mechanical vibrations in the nanometer to tens-of-nanometers displacement range and generates biomimetic spiking waveforms. Spike rate-encoding of the input amplitude is demonstrated, with output spiking frequencies tunable between approximately 100 Hz and 1 kHz depending on the excitation level. The waveform is finally converted to a biphasic shape suitable for cochlear implant stimulation. Through realizing temporal spike-encoding, a fundamental principle in the healthy auditory pathway, the proposed approach can provide significant benefits for cochlear implants. In addition, the circuit has the potential to reduce footprint, energy consumption, and latencies compared to current commercial solutions.

1. Introduction

Hearing loss affects millions of people worldwide, profoundly impacting communication, social interaction, and quality of life [1]. In 2019, over 403 million people had moderate to severe hearing loss, and this number is expected to nearly double by 2050 [2]. Cochlear implants (CIs) are medical devices designed to restore hearing in individuals with severe to profound sensorineural hearing loss by bypassing the damaged cochlea [3]. They are among the earliest human implants and are increasingly utilized globally. Although exact numbers are unknown, more than 170,000 people in the United States had undergone cochlear implantation by 2015 [4]. While cochlear implantation is more effective in prelinguistic children, its use in older populations is also rising [5]. Beyond its social impact, CIs have become the most significant medical market [6]. A standrad CI comprises an external microphone, a speech processor unit, a transmitter, and flexible electrodes with 12–22 channels that stimulate the auditory nerve directly [3] utilizing the tonotopic organization of the cochlea, where high-frequency signals are processed at the basal end and low-frequency signals are processed at the apical end of the cochlea [7]. While traditional CIs have significantly improved the quality of life for individuals with severe to profound hearing loss, they present several challenges [8], such as weak adhesion for patients with thick hair, social stigmatization due to visible external components, frequent battery replacements, and issues like pressure sores and electric discharge. Fully/totally implantable cochlear implants (FICI/TICI) address these drawbacks by eliminating external parts, enhancing aesthetic appeal, user convenience, and overall device performance.

However, the practical realization of FICI presents significant challenges. All implanted components must be fully biocompatible, compact, long-lasting, extremely low in power consumption, and immune

* Corresponding author at: Institute of Technical Physics and Materials Science, HUN-REN Centre for Energy Research, Konkoly-Thege M. út 29-33., Budapest, H-1121, Hungary.
E-mail address: torok.timea@ttk.bme.hu (T.N. Török).

https://doi.org/10.1016/j.bspc.2026.110761
Received 28 November 2025; Received in revised form 12 May 2026; Accepted 2 June 2026
Available online 10 June 2026

to internal noise, such as heartbeats or mechanical vibration from jaw movement or facial muscle contraction. In contrast to the earlier concepts, where a special microphone was implanted in the skull, Envoy Medical has recently introduced a more progressive solution by detecting the movement of one of the ossicle bones, the incus, in the middle ear and converting the processed signal into the cochlea by the same multielectrode [9]. The main advantage of this solution is that it is immune to the internal body noises. Moreover, it does not sacrifice or bypass the middle ear organ, which functions well for most CI recipients, and it also utilizes the middle ear to probe the vibrations that were efficiently captured by the eardrum, taking advantage of natural filtering and amplifying characteristics of the outer and middle ear. Although the concept outlines a credible strategy for next-generation FICIs, the energy-efficient signal processing is still an issue, especially if a non-chargeable implanted battery is used. This persistent challenge underscores the need for novel signal processing strategies that address energy-efficiency at the architectural level, paving the way for practical, energy-efficient FICIs with extended battery life and potentially longer operational lifetime.

The proposed architecture is built around three key components that together are designed to minimize power consumption and simplify auditory signal processing in fully implantable cochlear implants. These components include: (i) a Fast-Fourier Transformation (FFT)-free frequency-resolved cantilever array, (ii) piezoelectric analog-signal generation, and (iii) a compact neuromorphic spiking element capable of directly generating and encoding action potential-like bipolar signals. While the first two components have been detailed in our previous work [10], this paper focuses on the third component and its compatibility with the preceding elements.

Building on these components, the auditory sensing system operates as illustrated in Fig. 1: Vibroacoustic stimuli with multiple frequency components ($S = \sum S(f)$) are sensed by a MEMS cantilever array, each element tuned to different resonance frequencies $f_i^{\text{res.}}$, realizing frequency-selective sensing. The resulting electric signals are routed to a set of compact neuromorphic oscillators [11] which emit spiking signals proportional to the amplitude of the incoming stimulus in the ith channel, $f_i^{\text{osc.}} \sim S(f_i^{\text{res.}})$. This realizes frequency-selective rate-encoding across i channels and produces spike trains suitable for neuromorphic processing in FICIs.

To implement this neuromorphic spiking element, we employ resistive switching memories, or memristors. These elements are anticipated to be crucial components in next-generation neuromorphic circuits due to their memory effect, small footprint, low energy consumption, and negative differential resistance [12–19]. Non-volatile memristors show great promise for functioning as artificial synapses in spiking neural networks (SNNs) [20,21]. Volatile memristors, such as those constructed from VO_2 thin films, are excellent candidates for generating action potential signals, spiking/bursting patterns, or replicating several attributes of biological neurons, such as all-or-nothing firing, refractory period, spike frequency adaptation, and spike latency, thereby acting as artificial neurons [15,22,23]. A recent implementation of a VO_2 Mott memristor-based artificial spiking photoreceptor is reported in Ref. [24].

In this paper, we take advantage of the capabilities of VO_2 memristors to demonstrate, for the first time, the direct conversion of analog MEMS signals into biomimetic bipolar signals similar to biphasic signals used in commercial implants [3,25]. The mechanical excitation applied within a physiologically relevant nanometer-scale displacement range resembles the conditions inside the middle ear and is provided by a controlled source. Additionally, we demonstrate that the frequency of the generated spikes is proportional to the amplitude of the mechanical vibration, closely mimicking the human auditory system's temporal encoding of frequency-resolved signals [26].

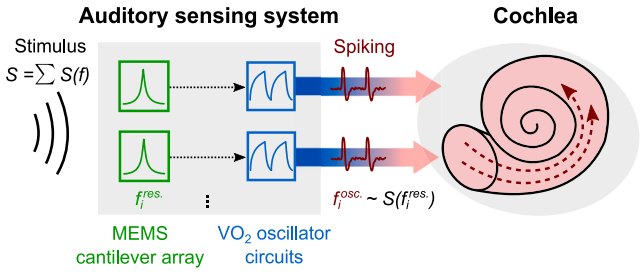

Fig. 1. Concept of our bio-inspired auditory sensing system. Vibroacoustic stimuli composed of several different frequency signals ($S = \sum S(f)$) are sensed by piezo-MEMS cantilevers, each having a well-defined resonance frequency, $f_i^{\text{res.}}$, realizing frequency-selective sensing. The output signals of the cantilever array are carried to VO_2 memristor-based relaxation oscillator circuits (i number of channels), which emit neural spikes proportional to the amplitude of the incoming stimulus in the ith channel, $f_i^{\text{osc.}} \sim S(f_i^{\text{res.}})$. The auditory sensing system realizes rate-encoding in i channels, creating spiking waveforms suitable for further processing by the nervous system, aimed at using in FICIs.

2. Methods

In this Section, we describe the measurement setup used for the characterization of MEMS cantilevers (Section 2.1), provide details on our VO_2 nanogap memristors and relaxation oscillators (Section 2.2), and validate our concept for an auditory sensing unit (i.e. one channel of the auditory sensing system shown in Fig. 1, see Section 2.3).

2.1. Characterization of piezoelectric MEMS cantilevers

The MEMS cantilevers used for our experiments incorporate a piezoelectric ScAlN layer [27] on a silicon-on-insulator platform. The spiral-shaped design of the cantilevers was optimized for the targeted application previously [10]. To emulate conditions inside the middle ear, the cantilevers were put under ~1 nm amplitude mechanical excitation, provided by the stage of a laser interferometric instrument (*SmarAct PicoScale Scanning Vibrometer*), capable of recording the displacement of the cantilever. In this setup, illustrated in Fig. 2a, the displacement is measured via the laser interferometric principle, and frequency spectra are recorded using the lock-in technique. Fig. 2b shows the custom-built sample holder used for the electromechanical characterization of the cantilevers. One important component of testing the presented concept for auditory sensing is providing biologically realistic, ~10 nm excitation, i.e., in the range of the movement of bones in the middle ear. Mechanical excitation was provided by a piezo shear actuator (*PI Ceramic P-142.03*), which has a sensitivity of 6 nm/V, and an axial resonant frequency of 120 kHz (far from the 200–700 Hz range under investigation). Nominal mechanical excitation amplitudes (stimuli) are calculated from the drive voltage amplitude of the piezoelectric actuator, based on the value of its 6 nm/V sensitivity. Electric signals of each cantilever are led through ribbon cables to custom PCBs on the two sides, where routing of each electrode is possible using two jumpers, leading the signal of a chosen cantilever to a pair of BNC connectors on the sides.

2.2. Memristor-based oscillators

The composition of VO_2 memristors is illustrated in Fig. 3a. For the fabrication of VO_2 memristors, 50 nm thick VO_2 layers were deposited on top of a sapphire (Al_2O_3) substrate, via pulsed laser deposition. Layers were prepared according to the procedure reported in Ref. [28], without any buffer layers between the single crystal Al_2O_3 substrate and the VO_2. Stoichiometry and epitaxial growth of the VO_2 layer were confirmed by scanning transmission electron microscopy – electron energy

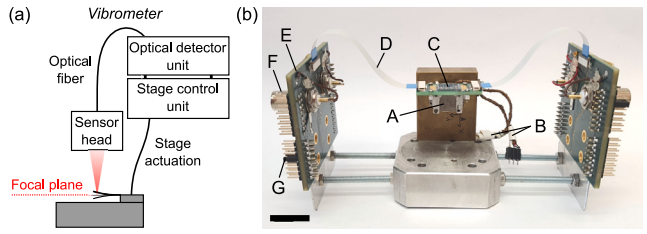

Fig. 2. Measurement setups for the characterization of piezo-MEMS cantilevers. (a) Schematics of the interferometric measurement setup used for the mechanical characterization of cantilevers. (b) Photo of the custom-built sample holder for the electromechanical test: (A) piezoelectric actuator, (B) shielded electrical connections to the piezoelectric actuator, (C) custom PCB holding the chip with cantilevers, (D) flexible ribbon cables to capture the cantilever's signal, (E) custom PCB for routing the connections to the cantilevers, (F) BNC connector, (G) jumper used for selecting the desired electrode of a cantilever. Scale bar: 2 cm.

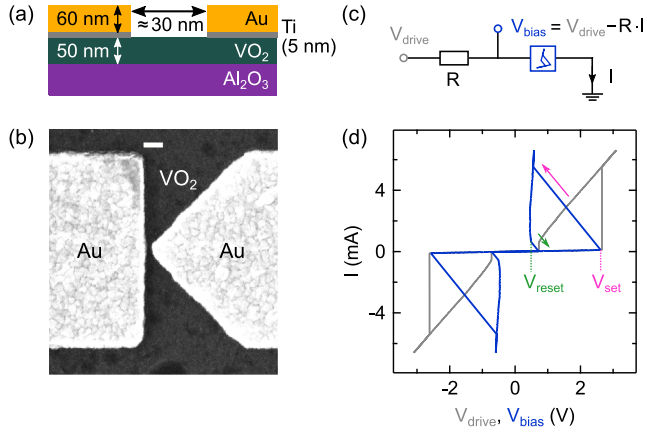

Fig. 3. Fabrication and characterization of VO_2 memristors. (a) Illustration of the planar memristor design showing layer thicknesses. (b) Scanning electron microscopy image of the nanogap region of a representative VO_2 device. Scale bar: 100 nm. (c) Circuit schematic for $I(V)$ characterization of the VO_2 samples. Drive voltage V_{drive} is applied to the memristor and a series resistor R, while current I is monitored. Bias voltage is calculated as $V_{bias} = V_{drive} - R \cdot I$. (d) Typical $I(V)$ curves of a VO_2 device exhibiting volatile resistance switching, R = 380 Ω. Current is also displayed as a function of bias voltage (blue curve) and drive voltage (gray curve). The set process/IMT (reset process/MIT) is indicated by a pink (green) arrow on the $I(V_{bias})$ curve. Note that these transitions are not resolved on the 12 kSa/s sampling rate of the measurement; there are no datapoints in the sections indicated with arrows.

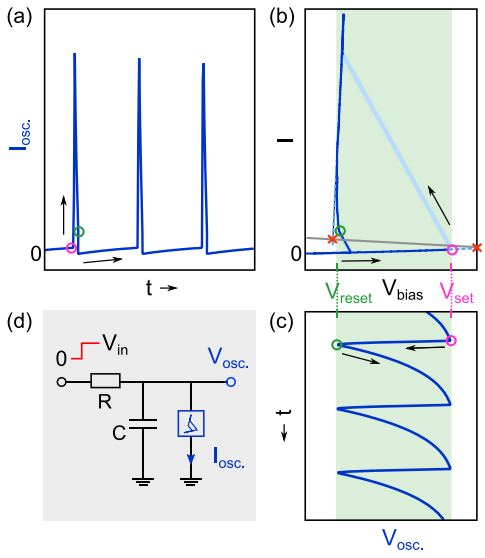

Fig. 4. Relaxation oscillator made of a VO_2 memristor. (a) Current waveform $I_{osc.}(t)$ of an oscillator. (b) Magnified $I(V_{bias})$ characteristics of a memristor (positive quadrant) shown with blue colors (transitions blurred with light blue). Gray line marks the possible equilibrium currents defined by the load line of the oscillator circuit according to the equation $(V_{in} - V_{bias})/R$. Equilibrium points defined by the continuation of the HRS and LRS are not reached, as marked by the red crosses. (c) Voltage waveform $V_{osc.}(t)$ of an oscillator. The green shaded area and pink/green labels of V_{set}/V_{reset} in panels (b–c) highlight the operation regime of the memristor during oscillation. Pink/green encircled points in panels (a–c) mark the points where set/reset transitions occur, and black arrows mark the direction. (d) Circuit schematics of the relaxation oscillator (output current/voltage and the memristor are highlighted in blue). Circuit element values were C = 611 nF and R = 15 kΩ throughout the measurements.

loss spectroscopy (STEM EELS) and X-ray diffraction measurements (XRD) [28–31].

On top of these epitaxial VO_2 layers, planar electrodes were deposited using electron-beam evaporation and lift-off techniques. The electrodes were patterned using standard electron-beam lithography (*Raith 150*), and 50 nm Au was evaporated after a 5 nm Ti adhesive layer deposition. Ultra-small gaps between electrodes in the 30–60 nm range were formed with this method. The layout of the electrodes is depicted in the electromicrograph of Fig. 3b, which shows a V-shaped electrode facing a flat one. This arrangement ensures the focusing of the electric field into a small, nanometer-sized active region. The development of memristors with such a planar, nanogap layout was reported in Ref. [32].

Resistive switching characteristics of the VO_2 nanogap memristors were studied in the simple circuit arrangement depicted in Fig. 3c. Slowly ramped (~1 Hz) triangular voltage signals, V_{drive}, are applied by a data acquisition card (National Instruments USB-6363) to an R = 380 Ω series resistor and the memristor. The applied voltage V_{drive} and the current I are measured using the same data acquisition card at 12 kSa/s sample rate, the latter is measured through a current amplifier (Femto DLPCA-200) in the 10^3 V/A gain setting. There was no dedicated electroforming applied to the VO_2 nanogap memristors. Fig. 3d shows typical DC $I(V)$ characteristics of a VO_2 nanogap memristor, the gray curve depicts raw $I(V_{drive})$ data, whereas the blue curve is the compensated $I(V_{bias})$ dependence of the memristor, where the bias voltage $V_{bias} = V_{drive} - R \cdot I$ is the voltage drop on the memristor. Initially, at low V_{bias} levels, the memristor is in its insulating, high resistance state (HRS) until the voltage drop on it reaches the threshold for the onset of resistance switching (set process, see V_{set} threshold in Fig. 3d). Once this threshold is reached, the memristor undergoes an insulator-to-metal transition (IMT, marked with a pink arrow), after which the memristor arrives in a conductive, metallic low resistance state (LRS). Upon decreasing the voltage, the memristor stays in its LRS until the V_{reset} threshold is reached (here we define V_{reset} on the $I(V_{bias})$ curve). Once V_{reset} is reached, the VO_2 memristor undergoes the reverse effect, metal-to-insulator transition (MIT, marked with a green arrow) is observed, and HRS is formed again. The different resistances observed in these states (typically $R_{LRS} \lessapprox 1$ kΩ and $R_{HRS} \approx 30$ kΩ [33]) are the result of a Mott-type phase transition accompanied by structural rearrangement of the VO_2 material. In these nanogap memristors, the mutual effects of the high electric field, which stems from the ultra-small, ≈30 nm active region, and Joule heating are responsible for operation [32].

A relaxation oscillator can be realized by connecting an RC-circuit in series with a VO_2 memristor (see Fig. 4). The circuit shown in Fig. 4d exhibits oscillating current $I_{osc.}$ (Fig. 4a) and voltage $V_{osc.}$ (Fig. 4b) signals while driven by a constant input voltage of V_{in}. During oscillation, the memristor switches back and forth between its LRS and

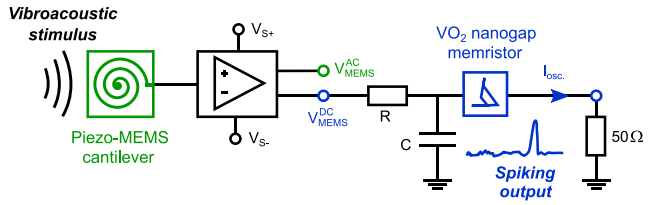

Fig. 5. Circuit schematics of a single channel of the proposed auditory sensing system. A piezo-MEMS cantilever with a well-defined frequency resonance senses a sinusoidal vibroacoustic stimulus provided at the same frequency. As a result, an AC voltage signal is generated by the cantilever, which is amplified (V^{AC}_{MEMS}) and rectified (V^{DC}_{MEMS}) by a custom-built circuitry. The V^{DC}_{MEMS} signal serves as an input DC voltage for the oscillator circuit, which emits current spikes at its output. These spikes are measured with the 50 Ω input terminal of a digital oscilloscope.

HRS. The points where the set (reset) transition happens are illustrated by pink (green) circles in Fig. 4a–c. Note, that during oscillation, the whole hysteresis curve of the memristor is walked around, which means, that $V_{osc.}$ varies between V_{set} and V_{reset} (see green shaded area and pink/green labels of V_{set}/V_{reset} in Fig. 4b–c).

To illustrate the conditions required for stable oscillations, the positive quadrant of the memristor's $I(V_{bias})$ curve in Fig. 3d is magnified in Fig. 4b. In this plot, set/reset transitions are blurred with a light blue color, since they are not resolved in DC measurements. With gray color, the load line of the oscillator circuit is shown, given by the equation $(V_{in} - V_{bias})/R$, which is a visualization of the possible equilibrium current flow in the circuit as a function of V_{bias}. The memristor would be in equilibrium if the load line intersected the HRS or LRS. Light blue dashed lines illustrate the continuation of these states, and red crosses mark their intersections with the load line; the current tends to reach these points in both states, but they are never reached since switching happens before that, which drives continuous oscillation.

The general role of circuit parameters affecting oscillatory behavior of a circuit depicted in the inset of Fig. 4d can be summarized as follows: (i) The series resistance R has to be chosen such that it ensures stable oscillation at the desired range of V_{in} input voltage levels (the load lines corresponding to V_{in} values do not cross HRS or LRS of the memristor); (ii) The parallel capacitance C can be used to tune the oscillation frequency of the circuit to the desired timescale. The timescales of the circuit are primarily governed by the RC time constants in the HRS and LRS of the memristor. Note that on the targeted, biologically relevant timescales in the ~ ms regime, the ~ps– ns timescales of resistance switching in VO_2 memristors [33,34] can be neglected, and switching can be considered as instantaneous. (iii) The input voltage level also affects the oscillation frequency. While R and C are constant, this dependence can be leveraged to realize encoding of V_{in} levels in oscillation frequency.

2.3. Concept validation

For validating our concept of the auditory sensing system shown in Fig. 1, we built and investigated the operation of a single channel according to the circuit depicted in Fig. 5. In our single-channel auditory sensing setup, a piezo-MEMS cantilever with a well-defined resonance frequency is driven by a sinusoidal vibroacoustic stimulus at the same frequency, generating an AC voltage. This signal is first amplified (V^{AC}_{MEMS}) and then rectified and smoothed to a DC level (V^{DC}_{MEMS}) by custom-made electronics designed for this purpose. The resulting V^{DC}_{MEMS} serves as an input to the VO_2 memristor-based oscillator circuit that produces output current spikes, which we record using the 50 Ω input of a digital oscilloscope.

To verify rate encoding of the circuit due to biologically relevant, ≈10 nm amplitude mechanical stimuli, we designed a custom setup for the precise control of the stimulus amplitude (see more details in Section 2.1 and in Fig. 2b). The operation of the circuit was also verified in less controlled experiments, where audio signals from a Bluetooth speaker were used as acoustic stimuli. Either a Picoscope 6404 A instrument (electromechanical experiments) or a Tektronix DPO 3014 digital oscilloscope (audio experiments) was used to record the output signals of the circuit.

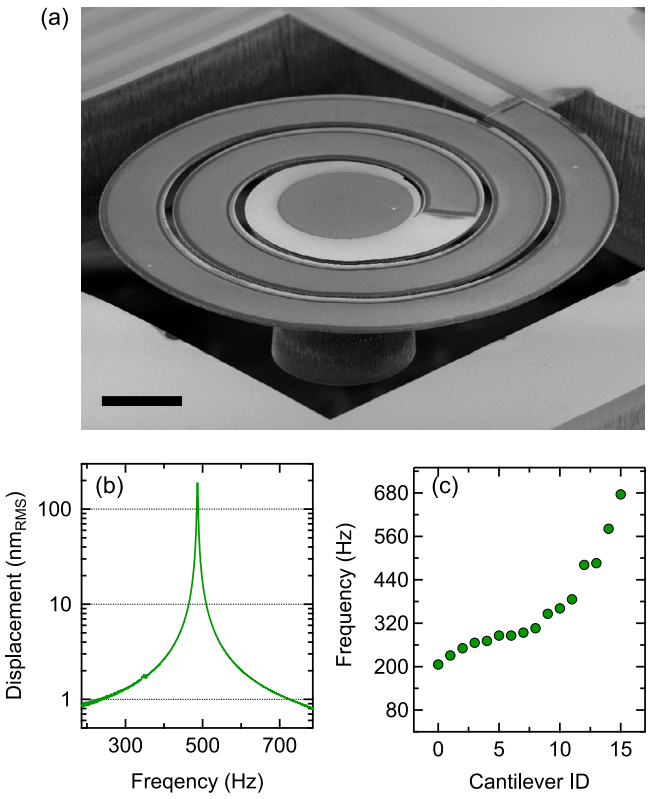

Fig. 6. Characterization of piezo-MEMS cantilevers. (a) Tilt-view scanning electron micrograph showing the typical geometry of a piezo-MEMS cantilever. Scale bar: 250 μm. (b) Displacement spectrum of a representative cantilever with $Q \approx 200$ quality factor and $f_r = 486$ Hz resonance frequency. (e) Resonance frequencies of the studied 16 cantilevers covering the 200–700 Hz frequency domain.

3. Results

3.1. Piezoelectric MEMS cantilevers

A scanning electron micrograph of an exemplary spiral-shaped cantilever is shown in Fig. 6a. The spiral is suspended at one side of a square cavity. The geometrical factors of the spirals, along with a seismic mass in the middle, determine their resonance frequencies [10]. The resonances are located at different frequencies, usually with $Q >$ 200 quality factor (see an exemplary resonance peak in Fig. 6b recorded in a laser interferometric measurement). The resonance frequencies of the 16 cantilevers with slightly different geometries cover the desired frequency range of 200–700 Hz (see Fig. 6c), where the fundamental frequencies of human speech are found. Conventional cochlear implants use 12–22 channels in the same frequency domain [3], being sufficient for speech recognition.

3.2. Spike generation and rate-encoding

First, the response of the auditory sensing circuit was analyzed using controlled electromechanical stimuli through a piezoelectric actuator.

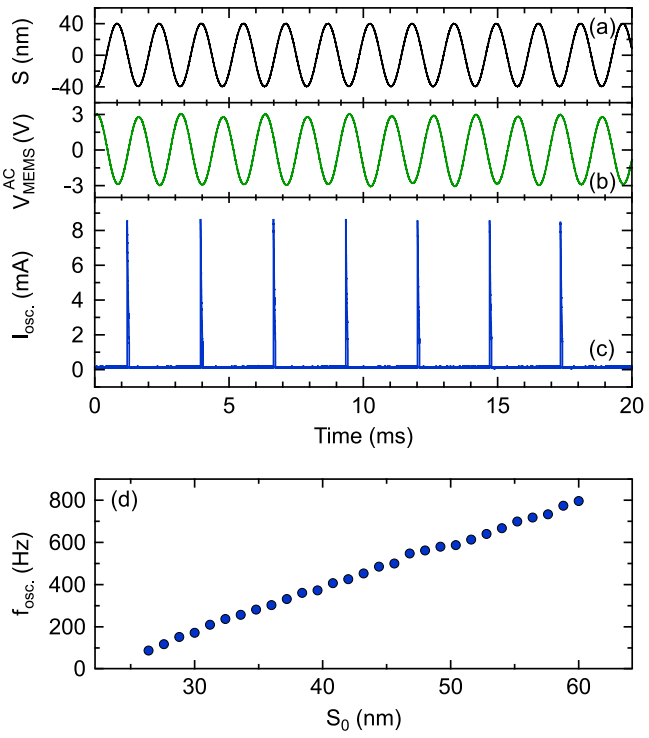

Fig. 7. Results of electromechanical experiments performed on a single-channel auditory sensing circuit, where stimulus to the cantilever is provided and controlled in the biorealistic displacement regime. (a) Waveform of a sinusoidal stimulus S, with constant frequency of 638 Hz. (b) Output signal V_{MEMS}^{AC} of the cantilever, conditioned to V_{MEMS}^{DC} = 3.6 V level, which drives the oscillator circuit. (c) Output current signal of the oscillator component exhibiting oscillation with a stable frequency. (d) Upon repeating experiments depicted in panels (a–c) with varying the stimulus amplitude S_0, we observed that the oscillation frequency $f_{osc.}$ depends linearly on S_0. Displacement values S are calculated from the voltage applied to the piezoelectric actuator and its 6 nm/V sensitivity. Within the oscillator part, component values were kept at C = 611 nF and R = 15 kΩ throughout the measurements.

The cantilever chip was mounted to the sample holder shown in Fig. 2b for these experiments. The V_{MEMS}^{DC} electric signal of a cantilever was utilized to drive an oscillator circuit according to the circuit schematics in Fig. 5.

The typical result of an experiment is shown in Fig. 7a–c, where a MEMS cantilever is excited at its 638 Hz resonance frequency with an S_0 = 40 nm amplitude sinusoidal stimulus (see black waveform S). Due to this excitation, the cantilever emits a similar sinusoidal output (see amplified green signal, V_{MEMS}^{AC}), which is conditioned to V_{MEMS}^{DC} = 3.6 V level, driving the oscillator component of the circuit. As a result, a spiking current signal with stable oscillation frequency $f_{osc.}$ appears at the output (see $I_{osc.}$ with blue in Fig. 7c). Note that $f_{osc.}$ is entirely independent from the frequency at which the cantilever is excited, since the amplifying circuitry completely smoothes out AC components. The spiking frequency $f_{osc.}$ is determined by (i) the values of R, C elements in the oscillator circuit, (ii) the device characteristics of the VO_2 memristor (threshold voltages of V_{set}, V_{reset} and resistance states R_{HRS}, R_{HRS}), and the (iii) input DC voltage level of the oscillator circuit (V_{MEMS}^{DC} in this experiment). The oscillator circuit's parameters (i–ii) can be adjusted such that the resulting spiking frequencies correspond to biologically relevant spike rates. Since the input DC voltage level also affects spiking frequency and depends on the amplitude of the incoming stimulus, this chain of dependencies can be utilized for spike rate-encoding of the incoming vibration amplitude.

Overall, by appropriately setting R and C values in the oscillator component, the frequency range of possible oscillations can be set

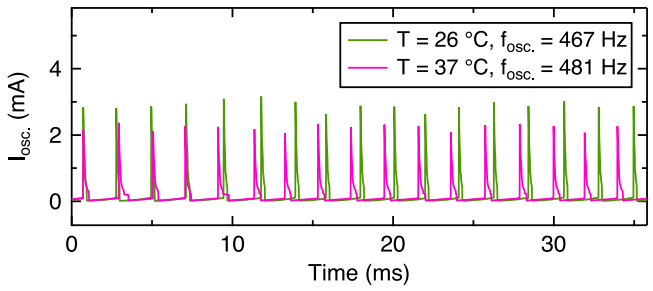

Fig. 8. Comparative measurement of a VO_2 oscillator at different temperatures. The oscillator was composed of C = 611 nF and R = 15 kΩ passive elements, and a VO_2 device was driven with V_{in} = 3 V DC voltage for 0.2 s-long intervals. The spiking waveform was recorded at room temperature (green curve) and then at physiological temperature (pink curve). Time axes are shifted to synchronize the signals and to show their slow divergence over a 35 ms time window. The resulting frequencies of 467 Hz and 481 Hz differ only by 3%.

to the desired ~1 kHz domain, where typical spiking rates of the auditory nerve are found [35,36]. Furthermore, this input voltage dependency enables encoding the stimulus amplitude S_0 in the frequency of output spikes, as shown in Fig. 7d, where this was verified by varying the amplitude of sinusoidal stimuli. In this experiment, the piezo-MEMS cantilever was excited at its 637 Hz resonance frequency, with amplitudes in the 26–60 nm range. In a realistic setting where the cantilever would be mounted near the umbo, these amplitudes correspond to 82–92 dB sound pressure levels [37]. The parameters of the oscillator were chosen such that the resulting spiking frequencies are found in the 100 Hz–800 Hz range, which is common in biological conditions. The information encoding shown in Fig. 7d resembles the natural encoding of sound amplitude in the nervous system, with similar frequency–amplitude characteristics as the sigmoid-shaped functions observable at the cellular level [38,39]. This rate-encoding behavior aligns with emerging FICI concepts, which increasingly rely on neural-inspired temporal coding strategies for efficient auditory signal representation [40].

To assess the feasibility of implantable operation, we performed spiking measurements at physiological temperature (37 °C) using the Mott oscillator circuit. A comparison with room-temperature operation is shown in Fig. 8. At 37 °C, the spiking waveform exhibits slightly longer relaxation tails due to the slower resistance relaxation of the memristor. However, the overall oscillation period becomes slightly shorter due to the decreased HRS of the memristor at elevated temperature, resulting in only a 3% increase in oscillation frequency (from 467 Hz to 481 Hz). This small deviation can be compensated by tuning the passive oscillator components. Since the temperature-induced effect is minimal, all subsequent measurements were performed at room temperature.

3.3. Shape-tuning of the excitation signal

CI devices should satisfy an essential safety requirement: the spiking waveform carried to auditory nerves should be bipolar (biphasic in CI terminology), yielding positive and negative sections as well. This bipolar waveform is needed to exclude the possibility of charge accumulation near the end of the implanted electrodes [3]. Current spikes at the output of a conventional VO_2 oscillator (see blue waveforms of Fig. 9a–b and corresponding circuit schematics in the top inset of Fig. 9c) are unipolar (monophasic in CI terminology), as they only have positive sections. Therefore, additional circuit elements are needed to convert this waveform into a bipolar signal. This conversion can be realized by adding a parallel LR circuit to the output (see bottom inset of Fig. 9c for schematics).

Table 1
Comparison of a conventional FFT/DSP (digital signal processing) based CI and the proposed MEMS/memristor-driven auditory sensing system for FICIs.

Feature	Conventional FFT/DSP CI	Proposed piezo-MEMS/VO_2 memristor FICI
Present maturity	Clinical standard	Single-channel proof of concept
Frequency analysis method	Digital FFT	Mechanical resonance of MEMS cantilevers
Power profile	ADC, DSP, memory, clocking, DAC, RF	Analog processing of MEMS signal
Power consumption	10–100 mW [41]	~640 μW (estimated for 16 channels)

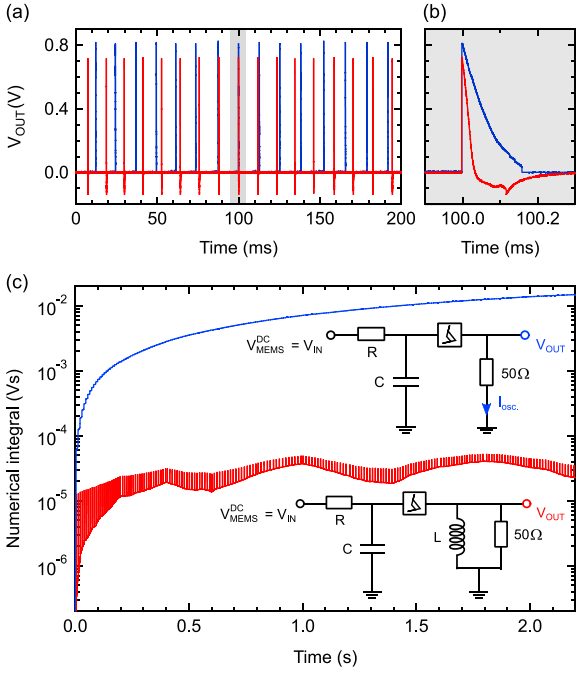

Fig. 9. Audio experiments with shape-tuning of the output waveform. (a) Comparison of output waveforms of the auditory sensing circuit built with a conventional oscillator (blue curve) and a modified oscillator (red curve). Only 200-ms-long sections of the 2.2-s-long measurements are shown; both waveforms are shifted such that a spike appears at 100 ms. (b) Plot is magnified on the time axis of the gray shaded area in panel (a) (the *y*-axis is the same as in panel (a)). (c) Comparison of numerical integrals calculated from the 2.2-s-long stimulation in case of the conventional oscillator (blue curve, see top inset for circuit schematics) and the modified oscillator (red curve, see bottom inset for circuit schematics) as the spiking component of the auditory sensing circuit. In the oscillator, $R = 15$ kΩ and $C = 611$ nF were kept constant, while an $L = 2.2$ mH inductor was added to the modified circuit.

In our experiments, where we investigated shape-tuning, a less-controlled acoustic stimulus from a Bluetooth speaker held close to the cantilever array was used to provide stimuli. First, the operation of the circuit with a conventional oscillator component was verified (see blue waveforms in Fig. 9a–b). Next, the appearance of a bipolar waveform was confirmed (see red signal in Fig. 9a and magnified waveform in Fig. 9b). This bipolar pulsed waveform has 0.7 V amplitude (for positive spikes) and 20 μs pulse duration. Considering typical electrode-tissue resistances of 2–10 kΩ [42], currents of 70–350 μA are feasible. Thereby, our waveform conforms with typical values in the 100 μA-range for the stimulating current and 10–200 μs for pulse duration, which is crucial for safe electrical stimulation of the cochlear nerve [43].

The obtained waveform (red curve in Fig. 9b) differs from the conventional rectangular pulses used in CI devices [3]; however, a study had shown that the usage of such ramped signals instead of rectangular ones (i) can induce similar electrically-evoked auditory brainstem response in mice, and (ii) could be more energy-efficient, having the potential to lower battery usage in CIs [25].

To demonstrate the difference between the cumulative effects of unipolar and bipolar signals, numerical integrals are calculated from 2 s-long experiments, shown in Fig. 9c. As expected, the integral of the unipolar signal increases monotonically (blue curve). In contrast, the bipolar signal shows no definitive tendency; the fluctuation around a small, non-zero value is an instrumental artifact from a low-frequency drift superimposed on the measured signal.

One of the most common complications of cochlear implant surgery is unintended facial nerve stimulation (FNS), which affects between 1%–15% of patients, resulting in discomfort and pain [44,45]. FNS can happen due to the facial nerve's close proximity to the cochlear lateral wall and is also associated with high stimulation levels [46]. According to clinical studies, the usage of charge-balanced monophasic signals (similar to the red waveform depicted in Fig. 9b) instead of common biphasic signals (having equal positive and negative sections) can ease the effects of FNS [47–50]. Hence, our proposed memristive auditory sensing circuit can also alleviate the effects of unintended FNS. Besides, the design of the *RL*-part providing the stimulus imposes a limitation on the maximum charge accumulating on the coil, which provides a protective limitation on the maximum current per spike during stimulation.

Beyond waveform characteristics, low power consumption is another critical requirement for fully implantable cochlear implants. The average power of the bipolar waveform (red trace in Fig. 9a–b) is estimated to be 0.14–1.4 μW, calculated from the product of the peak voltage (0.7 V), stimulation current (~100 μA), pulse width (20 μs), and oscillation frequency (~100–1000 Hz). In addition, the power consumption of the MEMS cantilever's amplification stage can be minimized using low-power amplifiers designed for implantable applications, reducing this contribution to ~40 μW (estimation based on 4 levels of amplification and calculating with capacitor leakage), dominating overall consumption. Calculating with 16 channels – a typical channel number in conventional cochlear implants – an average power in the range of 640 μW is estimated as the total consumption of an auditory sensing system utilizing piezo-MEMS cantilevers and VO_2 oscillators. This is significantly lower than the total power consumption of state-of-the-art digital FFT-based cochlear implant processors (~10–100 mW [41]), which also include RF communication and digital signal processing (DSP) blocks that are not required in our approach. A comparison of the main features of conventional CIs and our proposed auditory sensing system is presented in Table 1.

4. Conclusion and outlook

We proposed a concept for an auditory sensing system designed for use in FICIs. The operation of a single channel was tested and verified in electromechanical experiments with controlled mechanical stimuli. Our experiments demonstrate that the auditory sensing circuit is capable of emitting a spiking output in response to biologically realistic excitation amplitudes in the ~10 nm range and also capable of rate-encoding of the incoming stimulus amplitude, converting it to the 100 Hz–1 kHz output frequency domain. In our experiments where audio signals were used as stimuli, we showed that unipolar current spikes can conveniently be transformed to a charge-balanced bipolar waveform as a prerequisite to application in cochlear implants. The output pulses' amplitude and duration conform to typical values utilized in cochlear implants. The resulting waveform shape has the potential to alleviate the effects of

unintended facial nerve stimulation, reducing discomfort and pain in patients.

Beyond demonstrating the core operating principle, several practical aspects relevant to future implantable implementation should also be considered. For future clinical translation, the VO_2 device layer would be fully isolated from biological tissue by hermetic biocompatible packaging, for example, using a titanium casing with insulated feedthroughs, as commonly employed in implantable electronic devices [51,52]. Moreover, the amount of VO_2 used in our devices is extremely small, being deposited only locally in the nanogap region; thus, as in conventional Si-based chips that may contain non-biocompatible materials, the key requirement is not direct material biocompatibility but reliable encapsulation that prevents any contact with the physiological environment. Owing to the CMOS compatibility of both VO_2 memristors and AlN-based MEMS technology, monolithic integration on the same substrate appears feasible. In addition, system-in-package approaches, commonly employed in MEMS sensor technology, may also provide a practical route for heterogeneous integration of the different functional components.

Although operation was investigated only up to physiological temperatures in the present work, previous studies indicate that destabilization of the VO_2 oscillator only occurs when approaching the Mott transition temperature of VO_2 (~68 °C), at around 50 °C [33]. Since this temperature range lies well above physiological conditions, the thermal stability of the proposed oscillator concept is expected to be sufficient for implantable operation.

In addition to integration and thermal considerations, device-to-device variability also represents an important practical aspect of multichannel implementation. For the MEMS array, fabrication-induced variations can shift cantilever resonance frequencies, affecting the tonotopic map. However, their high Q factors enable post-fabrication measurement and calibration by assigning each channel based on its measured resonance. Similarly, variations in VO_2 memristors (e.g., V_{set}, V_{reset}, HRS/LRS) can alter oscillation characteristics. However, these quantities deviate only ≈15–30% from their respective average values across 70 devices [33]. This non-uniformity can be compensated by tuning the oscillator's R and C components, requiring channel-wise calibration. Such calibration is consistent with patient-specific fitting in cochlear implants, although long-term stability remains an important consideration for future implantable systems.

The demonstrated low-footprint and low-power operation can facilitate the application of the proposed auditory sensing circuit in fully implantable systems. The planar-type nanogap VO_2 memristors used in this study were shown to endure $>2 \cdot 10^{13}$ cycles of oscillations in our recent study involving 100 MHz-range oscillators [33]. This cycle number corresponds to approximately 634 years of continuous operation at a stimulation rate of 1 kHz, predicting a remarkably long lifetime for memristor-based spike encoder units. Taking the first 10% of the lifetime, corresponding to a 60-year interval, an ≈8% variation in frequency is experienced. For FICI applications, this means a slight shift in encoded sound volume over the years, similarly to the natural process of aging affecting loudness perception.

The proposed circuit may help to mitigate latencies of ≈10 ms typically experienced in commercial CI devices, i.e., the delay between the CI's electrical stimulation and the acoustic input, which has been shown to improve sound localization of patients [53]. In addition to the demonstrated rate-encoding approach, the proposed auditory circuit could also be adapted to support phase-locking through appropriate coupling of the MEMS output signal to the oscillator component. Since the auditory pathway inherently uses temporal information encoding principles like rate-encoding and phase-locking, applying these principles in cochlear implants can yield meaningful benefits [54].

While these perspectives highlight the potential of the proposed architecture, a few limitations of the present proof-of-concept should be acknowledged. The experiments validate a single auditory sensing channel, whereas a practical cochlear implant front end would require a multichannel array covering a substantially broader auditory frequency range. This could easily be delivered, since our auditory sensing circuit is scalable. There is a method routinely used in conventional CIs, the application of virtual channels [55], where intermediate frequencies are encoded by stimulating channels with adjacent frequencies simultaneously. Within our system, this approach would be feasible by decreasing the Q factors of the cantilevers, for which opportunities are limited. Once implanted, programmability in our system is inherently limited, which is generally challenging for all FICI concepts. Also, the shape of the stimulating waveform cannot be freely tuned independently of the shaping circuitry and the memristor/oscillator components.

Despite these limitations, the present results demonstrate the feasibility of an FFT-free, frequency-selective, memristor-driven auditory sensing architecture capable of biomimetic temporal spike encoding. The proposed concept provides a promising foundation for future multichannel, low-power, fully implantable cochlear implant front ends.

CRediT authorship contribution statement

Tímea Nóra Török: Writing – original draft, Visualization, Validation, Software, Methodology, Investigation, Data curation. **Roland Kövecs:** Writing – review & editing, Investigation. **Ferenc Braun:** Resources, Investigation. **Zsigmond Pollner:** Investigation. **Tamás Zeffer:** Investigation. **Nguyen Quoc Khánh:** Resources. **László Pósa:** Resources, Investigation. **Péter Révész:** Writing – review & editing. **Heungsoo Kim:** Resources. **Alberto Piqué:** Resources. **András Halbritter:** Writing – review & editing, Supervision, Resources, Funding acquisition. **János Volk:** Writing – original draft, Supervision, Resources, Project administration, Methodology, Investigation, Funding acquisition, Conceptualization.

Declaration of competing interest

The authors declare the following financial interests/personal relationships which may be considered as potential competing interests: Tímea Nóra Török reports financial support was provided by Hungarian Academy of Sciences. László Pósa reports financial support was provided by Hungarian Academy of Sciences. László Pósa reports financial support was provided by National Research Development and Innovation Office. András Halbritter reports financial support was provided by National Research Development and Innovation Office. János Volk reports financial support was provided by National Research Development and Innovation Office. If there are other authors, they declare that they have no known competing financial interests or personal relationships that could have appeared to influence the work reported in this paper.

Acknowledgments

This research was supported by the Ministry of Culture and Innovation and the National Research, Development and Innovation Office within the Quantum Information National Laboratory of Hungary (Grant No.2022-2.1.1-NL-2022-00004), and the NKFI K143169, K143282, NKKP-Advanced 153275, TKP EGA 16, and TKP2021-NVA-03 grants. L.P. and T.N.T. acknowledge the support of the János Bolyai Research Scholarship of the Hungarian Academy of Sciences.

Data availability

The data that support the findings of this study are available via the ARP Research Data Repository at https://hdl.handle.net/21.15109/ARP/NNEEQB.

References

[1] Z.-q. Zhang, et al., Bidirectional associations between sensorineural hearing loss and depression and anxiety: a meta-analysis, Front. Public Health 11 (2024) 1281689, http://dx.doi.org/10.3389/fpubh.2023.1281689, URL: https://www.frontiersin.org/articles/10.3389/fpubh.2023.1281689/full.

[2] L.M. Haile, et al., Hearing loss prevalence and years lived with disability, 1990–2019: findings from the Global Burden of Disease Study 2019, Lancet 397 (10278) (2021) 996–1009, http://dx.doi.org/10.1016/S0140-6736(21)00516-X, URL: https://linkinghub.elsevier.com/retrieve/pii/S014067362100516X.

[3] F.-G. Zeng, et al., Cochlear implants: System design, integration, and evaluation, IEEE Rev. Biomed. Eng. 1 (2008) 115–142, http://dx.doi.org/10.1109/RBME.2008.2008250, URL: https://ieeexplore.ieee.org/document/4664429/.

[4] A.M. Nassiri, D.L. Sorkin, M.L. Carlson, Current estimates of cochlear implant utilization in the United States, Otol. Neurotol. 43 (5) (2022) e558–e562, http://dx.doi.org/10.1097/MAO.0000000000003513, URL: https://journals.lww.com/10.1097/MAO.0000000000003513.

[5] U. Rosenhall, C. Hederstierna, E. Idrizbegovic, Otological diagnoses and probable age-related auditory neuropathy in "younger" and "older" elderly persons, Int. J. Audiol. 50 (9) (2011) 578–581, http://dx.doi.org/10.3109/14992027.2011.580786, URL: http://www.tandfonline.com/doi/full/10.3109/14992027.2011.580786.

[6] D.L. Sorkin, Cochlear implantation in the world's largest medical device market: Utilization and awareness of cochlear implants in the United States, Cochlear Implant. Int. 14 (sup1) (2013) S4–S12, http://dx.doi.org/10.1179/1467010013Z.00000000076, URL: http://www.tandfonline.com/doi/full/10.1179/1467010013Z.00000000076.

[7] G. Von Békésy, Experiments in Hearing, in: Experiments in Hearing, Mcgraw Hill, Oxford, England, 1960.

[8] N. Cohen, The totally implantable cochlear implant, Ear Hear. 28 (2) (2007) 100S–101S, http://dx.doi.org/10.1097/AUD.0b013e31803150f4, URL: https://journals.lww.com/00003446-200704001-00024.

[9] J.R. Dornhoffer, et al., Initial experiences with the envoy acclaim® fully implanted cochlear implant, J. Clin. Med. 12 (18) (2023) 5875, http://dx.doi.org/10.3390/jcm12185875, URL: https://www.mdpi.com/2077-0383/12/18/5875.

[10] P. Udvardi, et al., Spiral-shaped piezoelectric MEMS cantilever array for fully implantable hearing systems, Micromachines 8 (10) (2017) http://dx.doi.org/10.3390/mi8100311, URL: https://www.mdpi.com/2072-666X/8/10/311.

[11] G. Csaba, W. Porod, Coupled oscillators for computing: A review and perspective, Appl. Phys. Rev. 7 (1) (2020) 011302, http://dx.doi.org/10.1063/1.5120412.

[12] A. Sebastian, et al., Memory devices and applications for in-memory computing, Nature Nanotechnology 15 (2020) 529–544, http://dx.doi.org/10.1038/s41565-020-0655-z.

[13] Z. Wang, et al., Resistive switching materials for information processing, Nat. Rev. Mater. 5 (3) (2020) 173–195, http://dx.doi.org/10.1038/s41578-019-0159-3.

[14] S. Kumar, et al., Dynamical memristors for higher-complexity neuromorphic computing, Nat. Rev. Mater. 7 (7) (2022) 575–591, http://dx.doi.org/10.1038/s41578-022-00434-z.

[15] H. Liu, et al., Artificial neuronal devices based on emerging materials: Neuronal dynamics and applications, Adv. Mater. 35 (37) (2023) 2205047, http://dx.doi.org/10.1002/adma.202205047, URL: https://onlinelibrary.wiley.com/doi/abs/10.1002/adma.202205047.

[16] M.-K. Song, et al., Recent advances and future prospects for memristive materials, devices, and systems, ACS Nano 17 (13) (2023) 11994–12039, http://dx.doi.org/10.1021/acsnano.3c03505.

[17] Y. Huang, et al., Memristor-based hardware accelerators for artificial intelligence, Nat. Rev. Electr. Eng. 1 (5) (2024) 286–299, http://dx.doi.org/10.1038/s44287-024-00037-6, URL: https://www.nature.com/articles/s44287-024-00037-6.

[18] Z. Fang, et al., Recent progress on artificial spiking neurons based emerging electronic devices for neuromorphic perception and computation, Nano Res. (2026) http://dx.doi.org/10.26599/NR.2026.94908456, URL: https://www.sciopen.com/article/10.26599/NR.2026.94908456.

[19] S. Zhao, et al., Observation of three types of NDR in flexible VOx Mott memristors, Appl. Phys. Lett. 127 (8) (2025) 083502, http://dx.doi.org/10.1063/5.0272045.

[20] G. Zhou, et al., Volatile and nonvolatile memristive devices for neuromorphic computing, Adv. Electron. Mater. 8 (7) (2022) 2101127, http://dx.doi.org/10.1002/aelm.202101127, URL: https://onlinelibrary.wiley.com/doi/abs/10.1002/aelm.202101127.

[21] I. Boybat, et al., Neuromorphic computing with multi-memristive synapses, Nat. Commun. 9 (2018) 2514, http://dx.doi.org/10.1038/s41467-018-04933-y.

[22] W. Yi, et al., Biological plausibility and stochasticity in scalable VO_2 active memristor neurons, Nat. Commun. 9 (2018) 4661, http://dx.doi.org/10.1038/s41467-018-07052-w.

[23] J.-K. Han, et al., A review of artificial spiking neuron devices for neural processing and sensing, Adv. Funct. Mater. 32 (33) (2022) 2204102, http://dx.doi.org/10.1002/adfm.202204102, URL: https://onlinelibrary.wiley.com/doi/abs/10.1002/adfm.202204102.

[24] C.Y. Han, et al., A flexible artificial spiking photoreceptor enabled by a single VO2 mott memristor for the spike-based electronic retina, ACS Appl. Mater. Interfaces 16 (42) (2024) 57404–57411, http://dx.doi.org/10.1021/acsami.4c12874.

[25] C.A. Navntoft, J. Marozeau, T.R. Barkat, Ramped pulse shapes are more efficient for cochlear implant stimulation in an animal model, Sci. Rep. 10 (2020) URL: https://api.semanticscholar.org/CorpusID:211253757.

[26] M.A. Rutherford, H. von Gersdorff, J.D. Goutman, Encoding sound in the cochlea: from receptor potential to afferent discharge, J. Physiol. 599 (10) (2021) 2527–2557, http://dx.doi.org/10.1113/JP279189, URL: https://onlinelibrary.wiley.com/doi/abs/10.1113/JP279189.

[27] N.Q. Khánh, et al., Effect of process parameters on co-sputtered Al(1-x)ScxN layer's properties: Morphology, crystal structure, strain, band gap, and piezoelectricity, Mater. Sci. Semicond. Process. 169 (2024) 107902, http://dx.doi.org/10.1016/j.mssp.2023.107902, URL: https://www.sciencedirect.com/science/article/pii/S1369800123005954.

[28] H. Kim, et al., Strain effect in epitaxial VO2 thin films grown on sapphire substrates using SnO2 buffer layers, AIP Adv. 7 (10) (2017) 105116, http://dx.doi.org/10.1063/1.5004125.

[29] H. Kim, et al., Optimization of the semiconductor-metal transition in VO2 epitaxial thin films as a function of oxygen growth pressure, Appl. Phys. Lett. 104 (8) (2014).

[30] H. Kim, et al., Active terahertz metamaterials based on the phase transition of VO2 thin films, Thin Solid Films 596 (2015) 45–50, http://dx.doi.org/10.1016/j.tsf.2015.07.062.

[31] R.J. Suess, et al., Ultrafast phase transition dynamics in strained vanadium dioxide films, Adv. Mater. Interfaces 4 (22) (2017) 1700810, http://dx.doi.org/10.1002/admi.201700810.

[32] L. Pósa, et al., Interplay of thermal and electronic effects in the Mott transition of nanosized VO_2 phase change memory devices, ACS Appl. Nano Mater. 6 (11) (2023) 9137–9147, http://dx.doi.org/10.1021/acsanm.3c00150.

[33] Z. Pollner, et al., VO2 oscillator circuits optimized for ultrafast, 100 MHz-range operation, Adv. Electron. Mater. (2025) e00433, http://dx.doi.org/10.1002/aelm.202500433, URL: https://advanced.onlinelibrary.wiley.com/doi/abs/10.1002/aelm.202500433.

[34] S.W. Schmid, et al., Picosecond femtojoule resistive switching in nanoscale VO2 memristors, ACS Nano 18 (33) (2024) 21966–21974, http://dx.doi.org/10.1021/acsnano.4c03840.

[35] D. Pérez-González, M.S. Malmierca, Adaptation in the auditory system: an overview, Front. Integr. Neurosci. 8 (2014) 19, http://dx.doi.org/10.3389/fnint.2014.00019, URL: https://europepmc.org/articles/PMC3931124.

[36] I.C. Bruce, Y. Erfani, M.S.A. Zilany, A phenomenological model of the synapse between the inner hair cell and auditory nerve: Implications of limited neurotransmitter release sites, Hear. Res. 360 (2018) 40–54, http://dx.doi.org/10.1016/j.heares.2017.12.016, URL: https://www.sciencedirect.com/science/article/pii/S0378595517303696.

[37] M.A. Zurcher, et al., A MEMS capacitive accelerometer design as middle ear microphone based on ossicular chain micromechanic characterization at umbo for fully implantable cochlear prosthesis, Sensors Mater. 22 (2010) 297–312, URL: https://api.semanticscholar.org/CorpusID:14243550.

[38] C. Lenk, et al., in: M. Ziegler, T. Mussenbrock, H. Kohlstedt (Eds.), Bio-Inspired Information Pathways: From Neuroscience to Neurotronics, Springer International Publishing, 2023, pp. 287–315.

[39] L.A. Westerman, R.L. Smith, Conservation of adapting components in auditory-nerve responses, J. Acoust. Soc. Am. 81 (3) (1987) 680–691, http://dx.doi.org/10.1121/1.394836.

[40] J. Žák, et al., Model-based design of artificial zero power cochlear implant, Mechatronics 31 (2015) 30–41.

[41] H. Zhu, et al., High-performance wireless power and data transmission system for medical implant devices using ASK modulation, Energies 17 (3) (2024) 731, http://dx.doi.org/10.3390/en17030731, URL: https://www.mdpi.com/1996-1073/17/3/731.

[42] M. Yip, et al., Energy-efficient waveform for electrical stimulation of the cochlear nerve, Sci. Rep. 7 (2017) 13582, http://dx.doi.org/10.1038/s41598-017-13671-y, URL: https://pmc.ncbi.nlm.nih.gov/articles/PMC5648926/.

[43] R. Shannon, A model of safe levels for electrical stimulation, IEEE Trans. Biomed. Eng. 39 (4) (1992) 424–426, http://dx.doi.org/10.1109/10.126616, URL: https://ieeexplore.ieee.org/document/126616.

[44] S. Berrettini, et al., Facial nerve stimulation after cochlear implantation: our experience, Acta Otorhinolaryngol. Ital. 31 (1) (2011) 11–16.

[45] K. Hallin, et al., Cochlear implantation and facial nerve stimulation: Clinical and anatomic correlations, Laryngoscope (2025) http://dx.doi.org/10.1002/lary.70143, URL: https://onlinelibrary.wiley.com/doi/abs/10.1002/lary.70143.

[46] H. Hu, B. Kollmeier, M. Dietz, Reduction of stimulation coherent artifacts in electrically evoked auditory brainstem responses, Biomed. Signal Process. Control. 21 (2015) 74–81, http://dx.doi.org/10.1016/j.bspc.2015.05.015, URL: https://www.sciencedirect.com/science/article/pii/S1746809415001020.

[47] L. Gärtner, et al., Facial nerve stimulation in cochlear implant users – a matter of stimulus parameters? Cochlear Implant. Int. 23 (3) (2022) 165–172, http://dx.doi.org/10.1080/14670100.2022.2026025.

[48] S.T. Eitutis, et al., Management of severe facial nerve cross stimulation by cochlear implant replacement to change pulse shape and grounding configuration: A case-series, Otol. Neurotol. 43 (4) (2022) 452, http://dx.doi.org/10.1097/MAO.0000000000003493, URL: https://journals.lww.com/otology-neurotology/fulltext/2022/04000/management_of_severe_facial_nerve_cross.6.aspx.

[49] F. Danieli, et al., The effects of multi-mode monophasic stimulation with capacitive discharge on the facial nerve stimulation reduction in Young children with cochlear implants: Intraoperative recordings, J. Clin. Med. 12 (2) (2023) 534, http://dx.doi.org/10.3390/jcm12020534, URL: https://www.mdpi.com/2077-0383/12/2/534.

[50] M.A. Hyppolito, et al., Cochlear re-implantation with the use of multi-mode grounding associated with anodic monophasic pulses to manage abnormal facial nerve stimulation, Cochlear Implant. Int. 24 (2) (2023) 55–64, http://dx.doi.org/10.1080/14670100.2022.2157077.

[51] S.-H. Ahn, J. Jeong, S.J. Kim, Emerging encapsulation technologies for long-term reliability of microfabricated implantable devices, Micromachines 10 (8) (2019) 508, http://dx.doi.org/10.3390/mi10080508, URL: https://pmc.ncbi.nlm.nih.gov/articles/PMC6723304/.

[52] S. Seok, Polymer-based biocompatible packaging for implantable devices: Packaging method, materials, and reliability simulation, Micromachines 12 (9) (2021) 1020, http://dx.doi.org/10.3390/mi12091020, URL: https://pmc.ncbi.nlm.nih.gov/articles/PMC8470363/.

[53] M. Körtje, et al., Impact of processing-latency induced interaural delay and level discrepancy on sensitivity to interaural level differences in cochlear implant users, Eur. Arch. Otrhinolaryngol. 280 (12) (2023) 5241–5249, http://dx.doi.org/10.1007/s00405-023-08013-w, URL: https://pmc.ncbi.nlm.nih.gov/articles/PMC10620283/.

[54] D. Riss, et al., FS4, FS4-p, and FSP: A 4-month crossover study of 3 fine structure sound-coding strategies, Ear Hear. 35 (6) (2014) e272, http://dx.doi.org/10.1097/AUD.0000000000000063.

[55] W. Nogueira, et al., Loudness and pitch perception using dynamically compensated virtual channels, Hear. Res. 344 (2017) 223–234, http://dx.doi.org/10.1016/j.heares.2016.11.017, URL: https://www.sciencedirect.com/science/article/pii/S0378595516302374.